

## Ionic liquid modified graphene nanosheets anchoring manganese oxide nanoparticles as efficient electrocatalysts for Zn–air batteries†

Jang-Soo Lee, Taemin Lee, Hyun-Kon Song, Jaephil Cho\* and Byeong-Su Kim\*

Received 12th June 2011, Accepted 13th July 2011

DOI: 10.1039/c1ee01942b

Ionic liquid (IL) modified reduced graphene oxide (rGO–IL) nanosheets anchoring manganese oxide ( $\text{Mn}_3\text{O}_4$ ) are synthesized *via* a facile solution-based growth mechanism and applied to a Zn–air battery as an effective electrocatalyst for the oxygen reduction reaction (ORR). In this study, the IL moiety in these composites increases not only the conductivity of the system, but also the electrocatalytic activity compared to pristine rGO, together with the synergic effect of facilitating the ORR with the intrinsic catalytic activity of  $\text{Mn}_3\text{O}_4$ . Based on the Koutecky–Levich plot, we suggest that the ORR pathway of these composites is tunable with the relative amount of  $\text{Mn}_3\text{O}_4$  nanoparticles supported onto the graphene sheets; for example, the ORR mechanism of the system with a lower  $\text{Mn}_3\text{O}_4$  (19.2%) nanoparticle content is similar to a Pt/C electrode, *i.e.*, a one-step, quasi-4-electron transfer, unlike that with a higher  $\text{Mn}_3\text{O}_4$  (52.5%) content, which undergoes a classical two-step, 2-electron pathway. We also demonstrate the potential of these hybrid rGO–IL/ $\text{Mn}_3\text{O}_4$  nanoparticles as efficient catalysts for the ORR in the Zn–air battery with a maximum peak power density of  $120 \text{ mW cm}^{-2}$ ; a higher performance than that from commercial cathode catalysts.

### Introduction

Harvesting energy from green resources and developing suitable storage systems are the top priorities of current research in energy. Though the lithium-ion battery leads the market in the

field of energy storage, it is still actively investigated as an alternative energy storage system with higher energy and power density to meet various energy demands.<sup>1,2</sup> In that regard, Zn–air batteries have attracted much attention due to their high potential such as low-cost, relatively high capacity, facile nature of handling and processing, and environmental benignity.<sup>3–6</sup> Among the many issues for the development of next generation Zn–air batteries, it is essential to develop highly efficient and low-cost catalysts for oxygen reduction reaction (ORR).<sup>7</sup> Although Pt-based electrocatalysts have been traditionally employed to catalyze the ORR with a high efficiency,<sup>8–13</sup> manganese oxides are particularly attractive candidates due to their high catalytic activity, high abundance of Mn, high stability, low cost, and lack

Interdisciplinary School of Green Energy and School of NanoBioscience and Chemical Engineering, Ulsan National Institute of Science and Technology (UNIST), Ulsan, 689–798, Korea. E-mail: jpcho@unist.ac.kr; bskim19@unist.ac.kr; Fax: +82-52-217-2019; Tel: +82-52-217-2923

† Electronic Supplementary Information (ESI) available: XRD and TGA data, and current normalized with mass (Mn) of rGO–IL/ $\text{Mn}_3\text{O}_4$  (2 : 1) and (10 : 1); SEM and HR-TEM images of rGO–IL/ $\text{Mn}_3\text{O}_4$  (2 : 1). See DOI: 10.1039/c1ee01942b/

### Broader context

This article reports a systematic study of the surface engineering of graphene nanosheets by an ionic liquid moiety, demonstrating its utility in the controlled growth of nanoparticles as well as improving its conductivity and electrocatalytic activity in the oxygen reduction reaction (ORR), that is essential for potential applications in a Zn–air battery. Interestingly, based on the Koutecky–Levich plot, we find that the oxygen reduction pathway of these composites is tunable with the relative amount of  $\text{Mn}_3\text{O}_4$  nanoparticles supported on the graphene sheets. For example, the ORR mechanism of the system with a lower  $\text{Mn}_3\text{O}_4$  (19.2%) nanoparticle content is similar to the Pt/C electrode, *i.e.*, a quasi-one-step, 4-electron transfer, unlike that with a higher  $\text{Mn}_3\text{O}_4$  (52.5%) content which undergoes a classical two-step, 2-electron pathway. Most importantly, we demonstrate the potential of these hybrid rGO–IL/ $\text{Mn}_3\text{O}_4$  nanoparticles as efficient catalysts for the ORR in the Zn–air battery with a maximum peak power density of  $120 \text{ mW cm}^{-2}$ , which is higher than that of commercial cathode catalysts. With its high surface area and combined catalytic activity with nanoparticles anchored on, we believe this study should present an important step forward in utilizing graphene in electrochemical catalysts and open new possibilities in applications as alternative low-cost catalysts for metal-air batteries and alkaline fuel cells.

of environmental issues.<sup>14–21</sup> However, there are still obstacles in utilizing manganese oxides as an efficient ORR catalyst due to their intrinsically low electrical conductivity.<sup>22–24</sup>

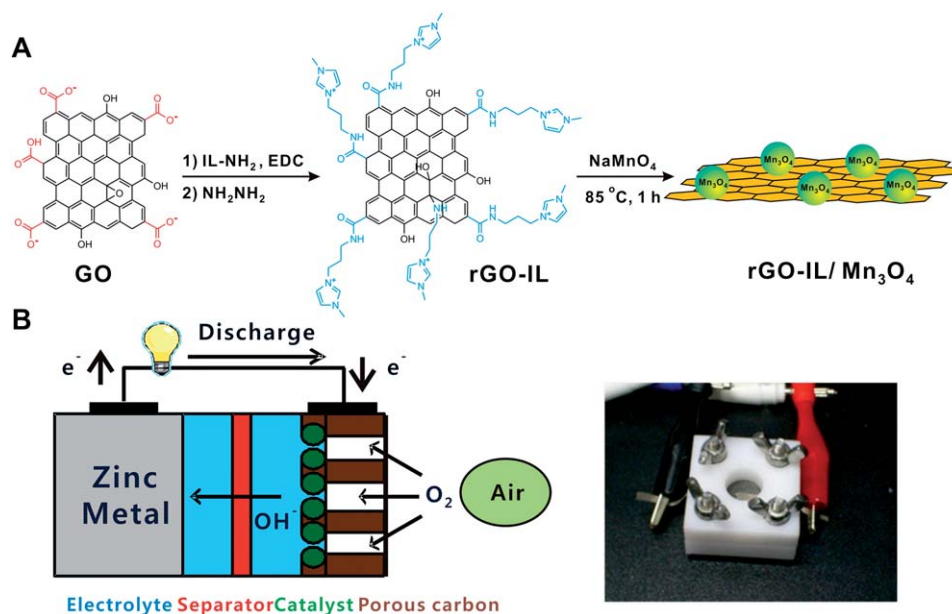
Graphene, a monolayer of aromatic carbon lattice, has recently drawn a tremendous amount of interest due to its extraordinary electrical, optical, thermal, and mechanical properties.<sup>25–30</sup> Taking full advantage of its chemical stability and high conductivity along with its high specific surface area, the graphene nanosheet is an excellent substrate for hosting and growing functional nanomaterials for high-performance electrochemical and electrocatalytic devices.<sup>31–33</sup> To date, a number of examples have been reported to host a variety of metal,<sup>34–38</sup> metal oxide,<sup>39–41</sup> semiconducting,<sup>42</sup> and magnetic nanoparticles<sup>43</sup> on the surface of graphene; however, up to now, few papers have reported the utilization of metal nanoparticles anchored on graphene and its catalytic activity in a Zn–air battery.

Herein, we present a simple approach of integrating manganese oxide nanoparticles into electrically conductive graphene sheets *via* a solution-based growth mechanism to afford hybrid graphene/Mn<sub>3</sub>O<sub>4</sub> nanoparticles (Scheme 1). Furthermore, we investigated their potential as an efficient electrocatalyst for the ORR in a Zn–air battery. In this study, we introduced the ionic liquid moiety onto the surface of graphene oxide with the aim of introducing the manganese oxide precursor on the surface of graphene as well as benefiting from the many features of the ionic liquid moiety (*i.e.* high ion conductivity, wide electrochemical windows, and the low interfacial energy between the graphene and the nanoparticles) that play a key role in enhancing the electrochemical activity of the resulting hybrid nanostructure.<sup>44</sup>

## Results and discussion

According to the modified Hummers method, graphite oxide suspensions were initially prepared from a commercial graphite

powder, followed by the sonication for the exfoliation of graphite oxide to graphene oxide (GO) nanosheets.<sup>45–49</sup> Carboxylic acid groups on the surface of GO were further reacted with 1-(3-aminopropyl)-3-methylimidazolium bromide (IL) through the *N*-ethyl-*N'*-(3-dimethyl aminopropyl)carbodiimide methiodide (EDC) mediated reaction to afford the ionic liquid moiety functionalized GO (GO–IL) (Scheme 1). As noted in other literature, the presence of the ionic liquid would enhance the solubility of graphene in a wide range of solvents,<sup>50</sup> facilitate its electrocatalytic activity and enhance its conductivity, hence improving overall the performance of the electrocatalyst. The successful functionalization of GO with the IL moiety was confirmed by zeta-potential measurements, which show a surface charge reversal from –52.0 mV to +45.2 mV upon functionalization. In addition, high-resolution X-ray photoelectron spectroscopy (XPS) further supported the presence of an IL moiety with the appearance of N1s 399.3 and 401.9 eV peaks from the imidazolium ring of ionic liquid (See ESI†). In order to restore the electrical conductivity of the pristine GO, chemical reduction of the GO–IL suspension was subsequently carried out by adding hydrazine to provide the reduced graphene oxide (rGO) nanosheets functionalized with the IL moiety (rGO–IL). In addition, manganese oxide nanoparticles were grown onto the above prepared rGO–IL nanosheets by a simple solution-based growth mechanism as shown in Scheme 1. Specifically, the manganese precursor, NaMnO<sub>4</sub>, was mixed through the electrostatic interactions in various feeding ratios (the ratio of rGO–IL to Mn precursor ranges from 1 to 20), followed by heating at 85 °C for 1 h. The relatively mild conditions are proved to be important to control the hydrolysis of the manganese precursor, which precludes the formation of free nanoparticles in solution. The resulting rGO–IL/Mn<sub>3</sub>O<sub>4</sub> composite was filtered and washed thoroughly with



**Scheme 1** (a) Schematic representation of the functionalization of the surface of graphene oxide and subsequent formation of nanoparticles. (b) Diagram of a Zn–air battery cell with a photograph of the actual cell tested.

deionized water and dried in the oven at 50 °C. The control experiment, carried out in the absence of rGO–IL under identical conditions, did not produce any nanoparticles that are redispersible in water.

The morphological structures of the rGO–IL/Mn<sub>3</sub>O<sub>4</sub> nanocomposites were characterized by scanning electron microscopy (SEM) and high-resolution transmission electron microscopy (HR-TEM). Based on the SEM and TEM images in Fig. 1, we found non-uniform coating of Mn<sub>3</sub>O<sub>4</sub> nanoparticles on the surface of graphene sheets possessing relatively spherical morphology with an average diameter of 9.45 ± 1.72 nm. HR-TEM images further reveal that crystal lattice fringes throughout the entire nanoparticles formed on the graphene sheet that matched with the major peaks of crystalline Mn<sub>3</sub>O<sub>4</sub> nanoparticles. The crystalline phase of manganese oxide nanoparticles

can be further revealed by the XRD spectrum, which clearly shows the formation of Mn<sub>3</sub>O<sub>4</sub> (ESI†). Moreover, the selected area electron diffraction (SAED) of the nanoparticles displays the crystalline nature of the Mn<sub>3</sub>O<sub>4</sub> nanoparticles that formed on the surface of the rGO–IL nanosheet. As shown in the elemental mapping of hybrid rGO–IL/Mn<sub>3</sub>O<sub>4</sub>, we observed the presence of the rGO–IL nanosheets by distinctive elements such as C, O and N as well as the presence of Mn<sub>3</sub>O<sub>4</sub> nanoparticles by Mn and O elements (Fig. 1f). Given the rather non-uniformly distributed Mn<sub>3</sub>O<sub>4</sub> nanoparticles on the surface of rGO–IL, we postulate that the ionic linkage between the surface of rGO–IL and the manganese precursor are possibly not uniformly distributed on the surface of graphene nanosheets. The graphene–nanoparticle interaction, however, allows good dispersion of Mn<sub>3</sub>O<sub>4</sub> nanoparticles grown on the rGO nanosheets thus avoiding the

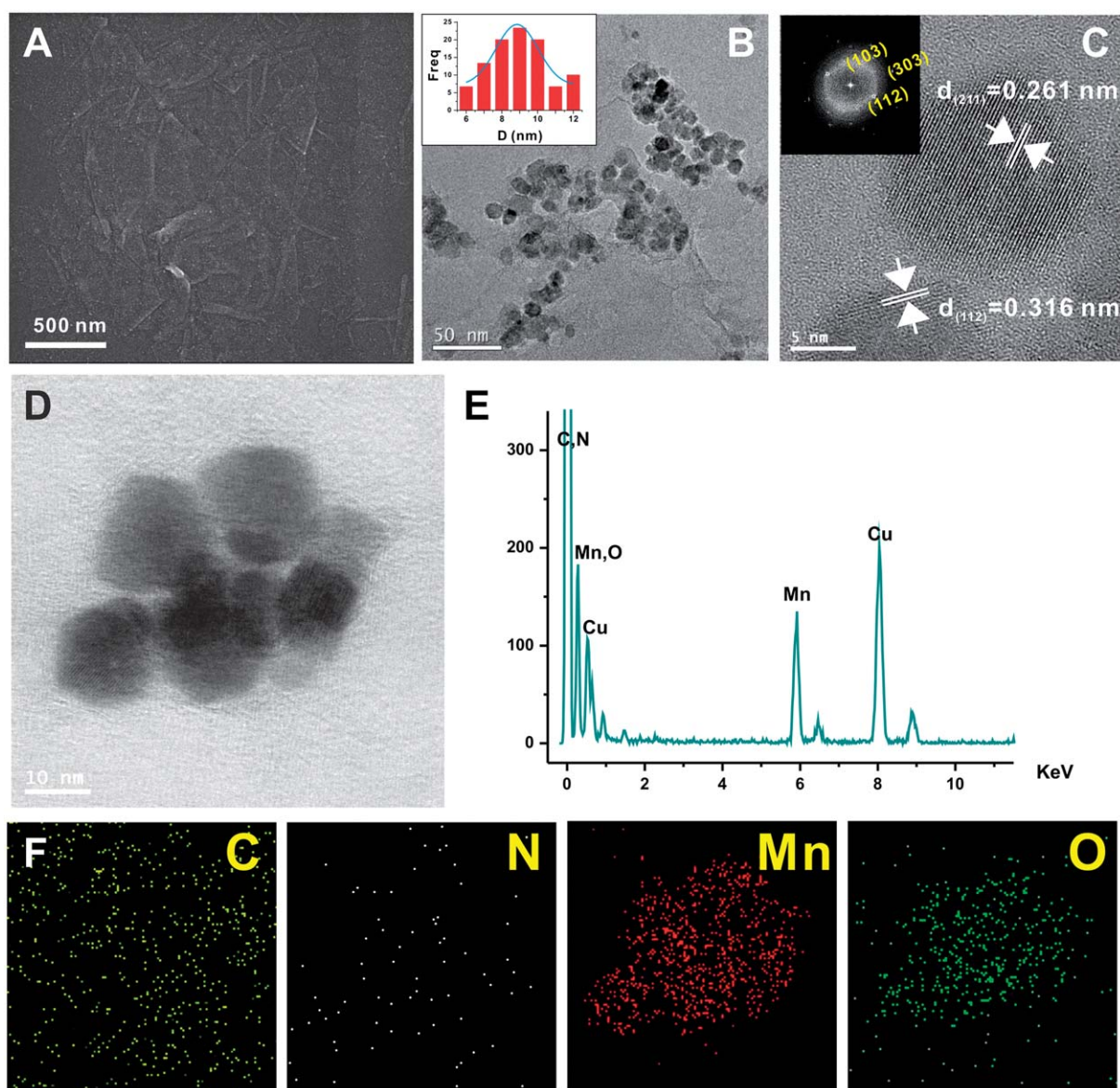


**Fig. 1** (a) SEM and (b) TEM images of rGO–IL/Mn<sub>3</sub>O<sub>4</sub> composites with size distribution of Mn<sub>3</sub>O<sub>4</sub> nanoparticles. (c) HR-TEM image of Mn<sub>3</sub>O<sub>4</sub> nanoparticles with the inset of the corresponding SAED pattern and (d, e, f) STEM and the EDX elemental mapping images of hybrid rGO–IL/Mn<sub>3</sub>O<sub>4</sub> (10 : 1) composites.

potential aggregation of nanoparticles during the electrocatalytic cycles.

With the hybrid nanoparticles prepared, we then performed the rotating-disk electrode (RDE) experiment to investigate the electrocatalytic activities of hybrid rGO-IL/Mn<sub>3</sub>O<sub>4</sub>. Since the electrons resulting from the oxidation of zinc metal should flow efficiently to the nanoparticle-supporting carbon substrate to reduce the oxygen during the actual operation of a Zn-air battery, the electrical conductivity together with the catalytic activity of the nanoparticles are critical factors in designing and developing the efficient catalyst.<sup>51</sup> Therefore, we employed two independent strategies to gain the insight on the catalytic activity: 1) chemical attachment of the ionic liquid moiety as well as chemical reduction of the graphene sheet to increase the conductivity of the system and electrocatalytic activity and 2) tuning the ratio of the Mn precursor with respect to the rGO-IL to determine the optimum ratio of our hybrid rGO-IL/Mn<sub>3</sub>O<sub>4</sub> catalyst for enhanced ORR activity while preserving necessary electrical conductivity. As shown in the Fig. 2, covalent attachment of the ionic liquid moiety onto the graphene nanosheet results in a higher limiting current and more positive onset potential than that of a plain, unmodified GO. This is consistent with the previous reports that the presence of the ionic liquid moiety would facilitate the electrocatalytic activity between the metal and oxygen,<sup>52</sup> as well as increase the solubility of the oxygen which can affect the enhanced reduction rate of oxygen to perhydroxyl or hydroxyl ions.<sup>53,54</sup>

Moreover, the chemically reduced graphene oxide (rGO-IL) has both a higher limiting current and more positive onset potential than GO-IL. Taken together, these data clearly support the critical role of the ionic liquid moiety as well as the enhanced conductivity gained upon the chemical reduction process of the GO nanosheet. Although electrical conductivity is another factor in determining ORR activity, the actual ORR activity of carbon materials is not sufficient to reduce oxygen effectively. When comparing the rGO-IL with rGO-IL/Mn<sub>3</sub>O<sub>4</sub> composites, the latter has a higher ORR activity as expected, among which rGO-IL/Mn<sub>3</sub>O<sub>4</sub> (10 : 1) has the highest catalytic activity. These results clearly show that Mn<sub>3</sub>O<sub>4</sub> nanoparticles facilitate the reaction effectively; however, higher Mn<sub>3</sub>O<sub>4</sub> contents (rGO-IL/Mn<sub>3</sub>O<sub>4</sub> (2 : 1), 52.5% Mn content as determined from TGA) can reduce ORR activity compared with a lower content of Mn<sub>3</sub>O<sub>4</sub> (rGO-IL/Mn<sub>3</sub>O<sub>4</sub> (10 : 1), 19.2% Mn

content) (See ESI for TGA data†). We postulate that the relatively larger content of Mn<sub>3</sub>O<sub>4</sub> with respect to the graphene sheet results in a lower electrical conductivity, which in turn, has an adverse effect on the ORR activity. This argument can be corroborated with the conductivity measurement with the 4-point probe. The sample with a lower content of Mn, rGO-IL/Mn<sub>3</sub>O<sub>4</sub> (10 : 1), displays a lower surface resistance of 61.1 ohm sq<sup>-1</sup> compared to 120.3 ohm sq<sup>-1</sup> of rGO-IL/Mn<sub>3</sub>O<sub>4</sub> (2 : 1). It is also of note that the absolute amount of Mn<sub>3</sub>O<sub>4</sub> in the hybrid is not the major factor in governing the ORR activity, since the limiting current normalized to the effective mass of active Mn<sub>3</sub>O<sub>4</sub> within the hybrid rGO-IL/Mn<sub>3</sub>O<sub>4</sub> yields approximately 4 times higher mass activity for the rGO-IL/Mn<sub>3</sub>O<sub>4</sub> (10 : 1) sample (-233.9 mA/mgMn at -0.45 V) than that of rGO-IL/Mn<sub>3</sub>O<sub>4</sub> (2 : 1) (-55.2 mA/mgMn at -0.45 V) (See ESI†).

To explore the ORR and the related kinetics in a more quantitative manner, we have further transformed the obtained RDE data based on the Koutecky-Levich equation (Fig. 3).<sup>55,56</sup> The Koutecky-Levich plot relates the current density (*i*) to the rotation rate of electrode ( $\omega$ ) to determine both the kinetic current (*i<sub>k</sub>*) and the number of transferred electrons (*n*) involved in the ORR.

$$\frac{1}{i} = \frac{1}{i_k} + \frac{1}{i_{dl}} = \frac{1}{i_k} + \frac{1}{B\omega} \quad (1)$$

$$i_k = nFAkC_{O_2} \text{ (kinetic current)} \quad (2)$$

$$i_{dl} = 0.20nFAC_{O_2}D_{O_2}^{2/3}\nu^{-1/6}\omega^{1/2} \text{ (diffusion limiting current)} \quad (3)$$

where *i<sub>k</sub>* represents the kinetic current; *i<sub>dl</sub>* is the diffusion limiting current; *n* is the number of electrons transferred per O<sub>2</sub> molecule; *F* is the Faraday constant (96485 C mol<sup>-1</sup>); *A* is the geometric area of the disk electrode (7.06 × 10<sup>-6</sup> m<sup>2</sup>); *k* (m s<sup>-1</sup>) is the rate constant for the ORR; *C<sub>O<sub>2</sub></sub>* is the saturated concentration of O<sub>2</sub> in solution (1.21 mol m<sup>-3</sup> in 0.10 M KOH);  $\nu$  is the kinematic viscosity (1 × 10<sup>-6</sup> m<sup>2</sup> s<sup>-1</sup> in 0.10 M KOH); *D<sub>O<sub>2</sub></sub>* is the diffusion coefficient of O<sub>2</sub> in solution (1.87 × 10<sup>-9</sup> m<sup>2</sup> s<sup>-1</sup> in 0.10 M KOH); and  $\omega$  is the angular frequency of the rotation (rad s<sup>-1</sup>). From the linear relationship between *i*<sup>-1</sup> vs.  $\omega^{-0.5}$  based on the Koutecky-Levich equation, we can obtain the number of electrons transferred (*n*) from the slope and compare the kinetic current (*i<sub>k</sub>*) from the intercept. Given the RDE data, we calculated the

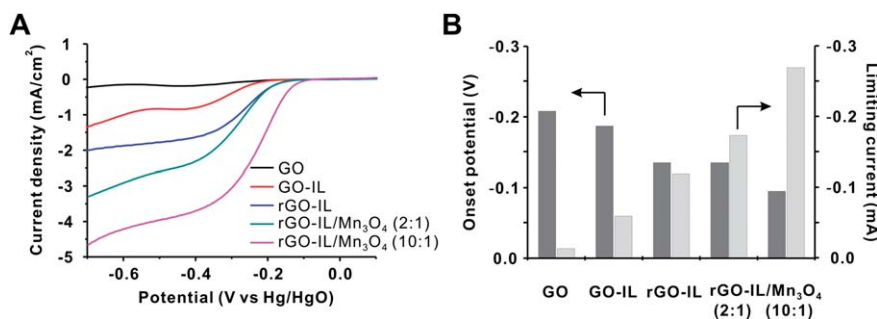


**Fig. 2** Rotating disk electrode (RDE) experiments of various samples prepared in this study. (a) Half-cell data and (b) comparison of the onset potential and limiting current of each sample of GO, GO-IL, rGO-IL, rGO-IL/Mn<sub>3</sub>O<sub>4</sub> (2 : 1), and rGO-IL/Mn<sub>3</sub>O<sub>4</sub> (10 : 1). The rotation rate is 3200 rpm and the scan rate is 10 mV s<sup>-1</sup>; 0.10 M KOH is used as an electrolyte. Pt wire and Hg/HgO are used as counter and reference electrodes with a 3 mm diameter working electrode, respectively. Onset potential was measured at -0.002 mA and limiting current was measured at -0.45 V.

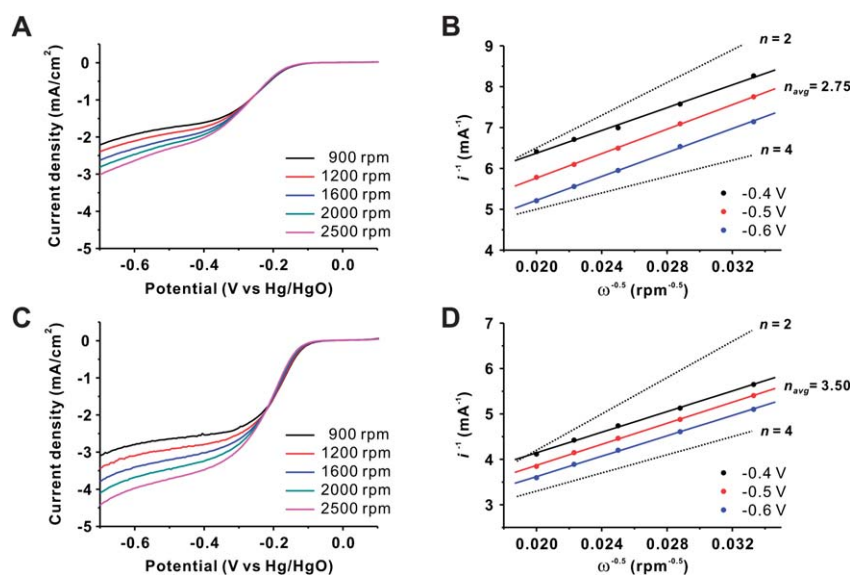


**Fig. 3** RDE experiments and the corresponding Koutecky–Levich plots of (a, b) rGO–IL/Mn<sub>3</sub>O<sub>4</sub> (2 : 1) and (c, d) rGO–IL/Mn<sub>3</sub>O<sub>4</sub> (10 : 1). The experiments were conducted at a scan rate of 10 mV s<sup>-1</sup> in an O<sub>2</sub>-saturated 0.10 M KOH solution. Theoretical slopes for  $n = 2$  and 4 are also constructed for comparison.

average number of electrons transferred from the samples of two different Mn<sub>3</sub>O<sub>4</sub> contents, particularly rGO–IL/Mn<sub>3</sub>O<sub>4</sub> (2 : 1) and (10 : 1). To our surprise, we found that the average number of transferred electrons ( $n$ ) of rGO–IL/Mn<sub>3</sub>O<sub>4</sub> (2 : 1) is 2.75 while it increased to 3.50 in the case of rGO–IL/Mn<sub>3</sub>O<sub>4</sub> (10 : 1). With these results, it is reasonable to estimate that there exist two independent mechanisms depending on the contents of Mn<sub>3</sub>O<sub>4</sub> in the hybrid rGO–IL/Mn<sub>3</sub>O<sub>4</sub> catalyst. Specifically, the corresponding number of electrons (3.50) for rGO–IL/Mn<sub>3</sub>O<sub>4</sub> (10 : 1) indicates an efficient one-step, quasi-4-electron transfer similar to the Pt/C electrode. On the other hand, the electron transfer number (2.75) of rGO–IL/Mn<sub>3</sub>O<sub>4</sub> (2 : 1) is close to the classical two-step, 2-electron pathway, as is the case for many other carbon-based electrode materials (Fig. 4). It is interesting to note that the reaction mechanism is tunable simply with the relative amount of nanoparticles supported onto the graphene sheets.

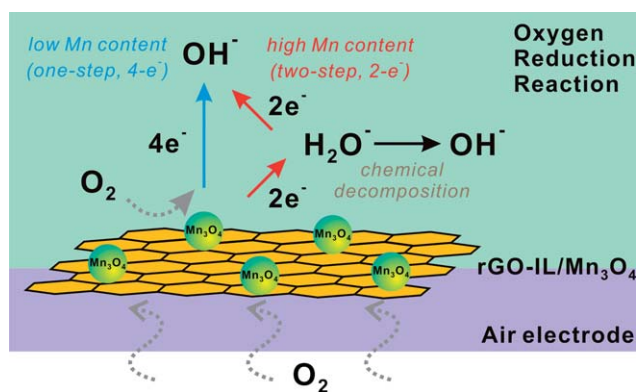


**Fig. 4** Schematic representation of the potential pathway of electrons during oxygen reduction reaction on the surface of rGO–IL/Mn<sub>3</sub>O<sub>4</sub> electrocatalysts.

Because the study on half-cell experiments such as RDE presents only the performance as a catalyst, we have to evaluate the actual ORR performance of catalysts in a Zn–air full cell. For that purpose, we have evaluated the electrochemical performance of a single Zn–air cell composed of an anode of zinc powder together with a hybrid rGO–IL/Mn<sub>3</sub>O<sub>4</sub> electrocatalyst in the cathode electrode.

Via a galvanodynamic method, the current density *versus* potential (reference to a Zn electrode) profile can be obtained under varying current density from 0 to 200 mA cm<sup>-2</sup> and one can calculate the maximum peak power density from a polarization curve for the Zn–air cell (Fig. 5). As shown in the discharge profile of Zn–air full cell, the voltage difference in two cells of different Mn contents rises significantly with the increase of current density. This result indicates that a resistance effect on a Zn–air cell is more dominant when high current density is applied to the cell and also coincides with the fact that the oxygen reduction reaction becomes very sluggish due to a high overpotential. When the power density plot is constructed, similar trends between RDE and actual cell performance are observed and maximum peak density of 120 mW cm<sup>-2</sup> can be obtained from the hybrid rGO–IL/Mn<sub>3</sub>O<sub>4</sub> (10 : 1) sample. For comparison, identical procedures were applied to compare the efficiency of the air cathode with the commercial gas diffusion electrode (GDE) including MnO<sub>x</sub> (Meet Inc., Korea) and 20% Pt on Vulcan XC-72 (E-TEK). Although the 20% Pt/C exhibits the best electrochemical performance among various samples, our hybrid rGO–IL/Mn<sub>3</sub>O<sub>4</sub> (10 : 1) still illustrates better efficiency in the overall Zn–air fuel cell performance than the commercial air cathode under the current density from 0 to 200 mA cm<sup>-2</sup>. With further improvements, we believe this hybrid catalyst could be used as a potential candidate in low-cost electrocatalysts for metal-air batteries and alkaline fuel cells. For more practical application of our hybrid catalyst in various electrocatalytic reactions, our

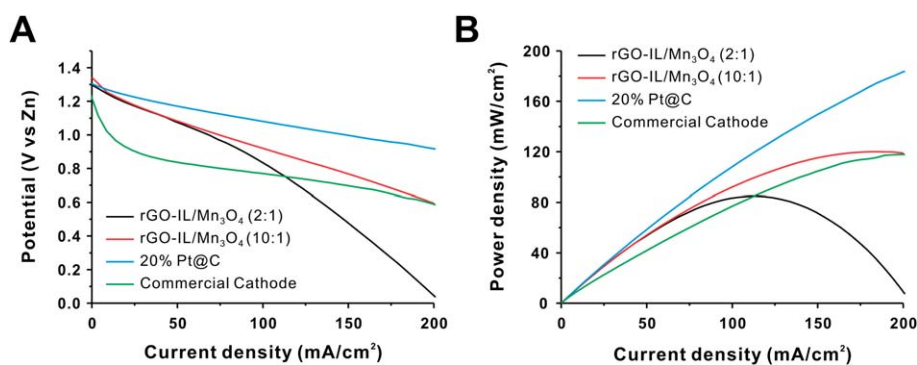


**Fig. 5** Single cell performance of the Zn–air battery assembled with hybrid rGO–IL/Mn<sub>3</sub>O<sub>4</sub> electrocatalysts compared with 20% Pt/C and commercial cathode materials. (a) Polarization curve of zinc-air cell and (b) corresponding power density plot of (black) rGO–IL/Mn<sub>3</sub>O<sub>4</sub> (2 : 1), (red) rGO–IL/Mn<sub>3</sub>O<sub>4</sub> (10 : 1), (blue) 20% Pt/C, and (green) commercial cathode (MEET) under the current density from 0 to 200 mA cm<sup>-2</sup>.

next endeavor should be focused more on addressing the stability and durability, as well as the product cost of the modified graphene nanosheet and hybrid catalyst.

## Conclusion

In summary, we present a simple and facile approach of integrating manganese oxide nanoparticles into the electrically conductive graphene sheets *via* a solution-based growth mechanism to afford hybrid graphene/Mn<sub>3</sub>O<sub>4</sub> nanoparticles. The ionic liquid moiety on the graphene nanosheet was proven to be important in enhancing the electrocatalytic activity of the hybrid nanoparticles in oxygen reduction reaction with a one-step, quasi-4-electron transfer pathway. By utilizing the high activity of the graphene/Mn<sub>3</sub>O<sub>4</sub> nanoparticles, we demonstrated their potential in the Zn–air battery, as they exhibit considerably high catalytic activity. By taking advantage of the facile synthetic nature of this hybrid nanoparticle with graphene nanosheet, we anticipate that the hybrid graphene/Mn<sub>3</sub>O<sub>4</sub> nanoparticles will open new possibilities in applications as alternative low-cost catalysts for metal-air batteries and alkaline fuel cells.

## Experimental

### Procedures of graphene oxide (GO) nanosheets

Graphite oxide was synthesized from graphite (Aldrich, <20 μm) by the modified Hummers method and exfoliated to give a stable, brown dispersion of graphene oxide (GO, typical conc. of 0.50 mg mL<sup>-1</sup>) under ultrasonication for 40 min and then centrifuged at 4000 rpm for 10 min to remove any aggregates remained in the suspension.

### Preparation of ionic liquid moiety (IL-NH<sub>2</sub>)

In the typical procedure according to the literature,<sup>47</sup> 3-bromopropylamine hydrobromide (1.1 g, 5.0 mmol) and 1-methylimidazole (0.395 mL, 5.0 mmol) were added to 15 mL ethanol, forming a colorless solution which was refluxed under nitrogen for 24 h. The resulting turbid mixture was purified by re-crystallization from ethanol, with ethyl acetate as an anti-solvent. Finally, the resulting white powder was dried under vacuum at 60 °C overnight and then purified.

### Preparation of ionic liquid modified graphene oxide nanosheet (GO–IL) and reduced graphene oxide nanosheet (rGO–IL)

Ionic liquid modified GO nanosheets (GO–IL) were prepared by reacting GO with excess IL-NH<sub>2</sub> (conc. 0.50 mg mL<sup>-1</sup>) under stirring for 5 h in the presence of *N*-ethyl-*N'*-(3-dimethyl amino-propyl) carbodiimide methiodide (EDC, 98%, Alfa Aesar). The resulting suspension was dialyzed (MWCO 12000–14000, SpectraPore) for a few days to remove any by product and residuals during functionalization. The prepared GO–IL suspensions exhibited a fairly good colloidal stability over a wide span of pH conditions. Chemical reduction of the GO–IL to rGO–IL was carried out by adding hydrazine as reported previously.

### Preparation of catalyst ink for rotating disk electrode

Catalyst ink was prepared by ultrasonically mixing 2.0 mg of as-prepared sample with 1.0 mL of pure deionized water for 1 h in order to make a homogeneous suspension. Then, 3 μL of the prepared catalytic ink was transferred to the surface of the 3 mm diameter glassy carbon electrode using a micropipette. Finally, the ink was dried for 10 min under vacuum conditions at room temperature to form a thin catalyst film on the glassy carbon electrode as a working electrode.

### Rotating disk electrode (RDE) experiments

All half cell experiments for the ORR using a rotating disk electrode (RDE) (ALS Co., Ltd) were carried out under the same conditions where Pt wire and Hg/HgO were used as a counter and a reference electrode respectively; 0.10 M KOH is used as an electrolyte; pure oxygen gas (99.9%) was purged for 30 min before each RDE experiment to make an electrolyte oxygen saturated condition. Rotation speeds were changed in this RDE measurement to deduce kinetic parameters related to ORR to construct the Koutecky–Levich plot. Electrochemical characterization of as-prepared catalysts were conducted using a single potentiostat (Ivium) with a scan rate of 10 mV s<sup>-1</sup> and potential range from 0.15 V to –0.7 V.

### Preparation of air electrode

All air electrodes used in this Zn–air full cell test are prepared with fixed weight composition; activated carbon (Darco G-60A,

Sigma-Aldrich) is 62 wt% + poly-tetrafluoroethylene (PTFE) binder 30 wt% (60 wt% PTFE emulsion in water, Sigma-Aldrich) + as-prepared catalysts is 8 wt%. After sonicating each material in pure DI-water for 1 h, each suspension was then mixed ultrasonically for 1 h to form a homogeneous suspension. The excess water is removed by filtering the homogeneous suspension and then the slurry is dried at 60 °C. By adding isopropyl alcohol to dried black powder, air electrodes were manufactured *via* a kneading and rolling process to make the desired thickness of air cathode. Finally, Ni-foam as a current collector was attached to the back side of the air electrode. The thickness of all air cathodes was set to 600 μm to minimize the thickness factor of electrodes to overall cell performance.

### Zn–air full cell assembly

For the Zn–air full cell test, homemade Zn–air single cell were used in this experiments. 1 g of zinc powder (Umicore) was used as the anode electrode. Nylon net filter (Millipore) was used as a separator. A 16–pi air electrode is used as the cathode electrode. The galvanodynamic experiment is carried out with a multichannel potentiostat (WBCS 3000, WonA Tech, Korea) with various current densities from 0 mA cm<sup>-2</sup> to 200 mA cm<sup>-2</sup> to characterize the Zn–air single cell performance.

### Acknowledgements

This research was supported by the WCU (World Class University) program through the Korea Science and Engineering Foundation funded by the Ministry of Education, Science and Technology (R31-2008-000-20012-0) and by the MKE (The Ministry of Knowledge Economy), Korea, under the ITRC (Information Technology Research Center) support program supervised by the NIPA (National IT Industry Promotion Agency, NIPA-2011-C1090-1100-0002).

### References

- 1 M. Armand and J. M. Tarascon, *Nature*, 2008, **451**, 652.
- 2 J.-S. Lee, S. Tai Kim, R. Cao, N.-S. Choi, M. Liu, K. T. Lee and J. Cho, *Adv. Energy Mater.*, 2011, **1**, 34.
- 3 F. R. McLarnon and E. J. Cairns, *J. Electrochem. Soc.*, 1991, **138**, 645.
- 4 P. Arora and Z. J. Zhang, *Chem. Rev.*, 2004, **104**, 4419.
- 5 T. Wang, M. Kaempgen, P. Nopphawan, G. Wee, S. Mhaisalkar and M. Srinivasan, *J. Power Sources*, 2010, **195**, 4350.
- 6 X. Li, A. L. Zhu, W. Qu, H. Wang, R. Hui, L. Zhang and J. Zhang, *Electrochim. Acta*, 2010, **55**, 5891.
- 7 K. Kinoshita, *Electrochemical Oxygen Technology*; Wiley & Sons: New York, 1992.
- 8 V. R. Stamenkovic, B. Fowler, B. S. Mun, G. Wang, P. N. Ross, C. A. Lucas and N. M. Markovic, *Science*, 2007, **315**, 493.
- 9 J. Zhang, M. B. Vukmirovic, K. Sasaki, A. U. Nilekar, M. Mavrikakis and R. R. Adzic, *J. Am. Chem. Soc.*, 2005, **127**, 12480.
- 10 J. Greeley, I. E. L. Stephens, A. S. Bondarenko, T. P. Johansson, H. A. Hansen, T. F. Jaramillo, J. Rossmeisl, Chorkendorff and J. K. Nørskov, *Nat. Chem.*, 2009, **1**, 552.
- 11 B. Lim, M. Jiang, P. H. C. Camargo, E. C. Cho, J. Tao, X. Lu, Y. Zhu and Y. Xia, *Science*, 2009, **324**, 1302.
- 12 K. Lee, M. Kim and H. Kim, *J. Mater. Chem.*, 2010, **20**, 3791.
- 13 J. Zhang, M. B. Vukmirovic, Y. Xu, M. Mavrikakis and R. R. Adzic, *Angew. Chem., Int. Ed.*, 2005, **44**, 2132.
- 14 J. P. Brenet, *J. Power Sources*, 1979, **4**, 183.
- 15 L. Mao, D. Zhang, T. Sotomura, K. Nakatsu, N. Koshiba and T. Ohsaka, *Electrochim. Acta*, 2003, **48**, 1015.

- 16 I. Roche, E. Chainet, M. Chatenet and J. Vondrák, *J. Phys. Chem. C*, 2006, **111**, 1434.
- 17 I. Roche, E. Chainet, M. Chatenet and J. Vondrák, *J. Appl. Electrochem.*, 2008, **38**, 1195.
- 18 F. Cheng, J. Shen, W. Ji, Z. Tao and J. Chen, *ACS Appl. Mater. Interfaces*, 2009, **1**, 460.
- 19 W. Xiao, D. Wang and X. W. Lou, *J. Phys. Chem. C*, 2009, **114**, 1694.
- 20 Y. Gorlin and T. F. Jaramillo, *J. Am. Chem. Soc.*, 2010, **132**, 13612.
- 21 V. Neburchilov, H. Wang, J. J. Martin and W. Qu, *J. Power Sources*, 2010, **195**, 1271.
- 22 H. Kim and B. N. Popov, *J. Electrochem. Soc.*, 2003, **150**, D56.
- 23 E. Raymundo-Pinero, V. Khomenko, E. Frackowiak and F. Beguin, *J. Electrochem. Soc.*, 2005, **152**, A229.
- 24 L. L. Zhang, T. Wei, W. Wang and X. S. Zhao, *Microporous Mesoporous Mater.*, 2009, **123**, 260.
- 25 K. S. Novoselov, A. K. Geim, S. V. Morozov, D. Jiang, Y. Zhang, S. V. Dubonos, I. V. Grigorieva and A. A. Firsov, *Science*, 2004, **306**, 666.
- 26 A. K. Geim and K. S. Novoselov, *Nat. Mater.*, 2007, **6**, 183.
- 27 J. Wu, W. Pisula and K. Müllen, *Chem. Rev.*, 2007, **107**, 718.
- 28 K. S. Kim, Y. Zhao, H. Jang, S. Y. Lee, J. M. Kim, K. S. Kim, J. H. Ahn, P. Kim, J. Y. Choi and B. H. Hong, *Nature*, 2009, **457**, 706.
- 29 S. Park and R. S. Ruoff, *Nat. Nanotechnol.*, 2009, **4**, 217.
- 30 V. C. Tung, M. J. Allen, Y. Yang and R. B. Kaner, *Nat. Nanotechnol.*, 2009, **4**, 25.
- 31 S. J. Guo, D. Wen, Y. M. Zhai, S. J. Dong and E. K. Wang, *ACS Nano*, 2010, **4**, 3959.
- 32 H. L. Wang, L. F. Cui, Y. A. Yang, H. S. Casalongue, J. T. Robinson, Y. Y. Liang, Y. Cui and H. J. Dai, *J. Am. Chem. Soc.*, 2010, **132**, 13978.
- 33 Y. Sun, Q. Wu and G. Shi, *Energy Environ. Sci.*, 2011, **4**, 1113.
- 34 G. M. Scheuermann, L. Rumi, P. Steurer, W. Bannwarth and R. Mülhaupt, *J. Am. Chem. Soc.*, 2009, **131**, 8262.
- 35 Y. Fang, S. Guo, C. Zhu, Y. Zhai and E. Wang, *Langmuir*, 2010, **26**, 11277.
- 36 W. Hong, H. Bai, Y. Xu, Z. Yao, Z. Gu and G. Shi, *J. Phys. Chem. C*, 2010, **114**, 1822.
- 37 Y. Li, X. Fan, J. Qi, J. Ji, S. Wang, G. Zhang and F. Zhang, *Nano Res.*, 2010, **3**, 429.
- 38 S. Zhang, Y. Shao, H. Liao, M. H. Engelhard, G. Yin and Y. Lin, *ACS Nano*, 2011, **5**, 1785.
- 39 D. Wang, D. Choi, J. Li, Z. Yang, Z. Nie, R. Kou, D. Hu, C. Wang, L. V. Saraf, J. Zhang, I. A. Aksay and J. Liu, *ACS Nano*, 2009, **3**, 907.
- 40 D. Wang, R. Kou, D. Choi, Z. Yang, Z. Nie, J. Li, L. V. Saraf, D. Hu, J. Zhang, G. L. Graff, J. Liu, M. A. Pope and I. A. Aksay, *ACS Nano*, 2010, **4**, 1587.
- 41 H. Jiang, L. Yang, C. Li, C. Yan, P. S. Lee and J. Ma, *Energy Environ. Sci.*, 2011, **4**, 1813.
- 42 G. Williams and P. V. Kamat, *Langmuir*, 2009, **25**, 13869.
- 43 H. He and C. Gao, *ACS Appl. Mater. Interfaces*, 2010, **2**, 3201.
- 44 J. F. Wishart, *Energy Environ. Sci.*, 2009, **2**, 956.
- 45 W. S. Hummers and R. E. Offeman, *J. Am. Chem. Soc.*, 1958, **80**, 1339.
- 46 G. Eda, G. Fanchini and M. Chhowalla, *Nat. Nanotechnol.*, 2008, **3**, 270.
- 47 D. Li, M. B. Muller, S. Gilje, R. B. Kaner and G. G. Wallace, *Nat. Nanotechnol.*, 2008, **3**, 101.
- 48 T.-K. Hong, D. W. Lee, H. J. Choi, H. S. Shin and B.-S. Kim, *ACS Nano*, 2010, **4**, 3861.
- 49 D. W. Lee, T.-K. Hong, D. Kang, J. Lee, M. Heo, J. Y. Kim, B.-S. Kim and H. S. Shin, *J. Mater. Chem.*, 2011, **21**, 3438.
- 50 H. F. Yang, C. S. Shan, F. H. Li, D. X. Han, Q. X. Zhang and L. Niu, *Chem. Commun.*, 2009, 3880.
- 51 Y. Zhang, Y. Shen, J. Yuan, D. Han, Z. Wang, Q. Zhang and L. Niu, *Angew. Chem., Int. Ed.*, 2006, **45**, 5867.
- 52 B. Li, H. Cao, J. Shao, M. Qu and J. H. Warner, *J. Mater. Chem.*, 2011, **21**, 5069.
- 53 J. Snyder, T. Fujita, M. W. Chen and J. Erlebacher, *Nat. Mater.*, 2010, **9**, 904.
- 54 Z. Wang, R.-M. Latonen, C. Kvarnström, A. Ivaska and L. Niu, *Materials*, 2010, **3**, 672.
- 55 A. J. Bard, L. R. Faulkner, *Electrochemical Methods*; Wiley & Sons: New York, 1980.
- 56 S. Treimer, A. Tang and D. C. Johnson, *Electroanalysis*, 2002, **14**, 165.